ACCSCIENCE PUBLISHING

International Journal of Bioprinting

RESEARCH ARTICLE

A generalized printing process window for preventing surface overcuring in volumetric additive manufacturing

Yifei Wang, Feng Chen*, Miaomiao Yuan, Wei Zhu, Yangguang Zhao, Ling Li, and Xiaoxiao Han

College of Mechanical and Vehicle Engineering, Hunan University, Changsha, Hunan, China

Abstract

Surface overcuring in volumetric additive manufacturing (VAM) occurs when material, process, and hardware parameters are not properly coordinated, leading to unintended polymerization near the vat boundary and impaired printability. Here, we develop a generalized theoretical model to predict the spatial light-dose distribution within rotating ink and to investigate the effects of key physical parameters, including projection beam size, vat dimensions, occlusion size, and material absorbance, on the onset of surface overcuring. The results show that this defect can be effectively suppressed through the synergistic regulation of these parameters. Specifically, lower material absorbance, smaller vat diameters, and narrower projection beams concentrate higher light energy in the central region of the vat while reducing energy deposition near the sidewalls, thereby promoting earlier solidification in the target region and preventing surface overcuring. Based on this model, a printing process window for suppressing surface overcuring is established as a quantitative guide for the design and fabrication of complex structures by VAM. The practical utility of this process window is further demonstrated through the successful fabrication of functional pH-responsive single- and multi-material drug delivery systems with controllable drug-release profiles. Overall, this study expands the printable design space of VAM for complex three-dimensional structures and provides a practical framework for more advanced applications.

Keywords: Volumetric additive manufacturing; Surface overcuring; Theoretical model; pH-responsive drug release; Multi-material fabrication

***Corresponding author:**
Feng Chen
(fchen@hnu.edu.cn)

Citation: Wang Y, Chen F, Yuan M, *et al*. A generalized printing process window for preventing surface overcuring in volumetric additive manufacturing. *Int J Bioprint*. 2026;12(3):026140128. doi: 10.36922/IJB026140128

Received: April 2, 2026

Revised: May 7, 2026

Accepted: May 11, 2026

Published online: May 11, 2026

1. Introduction

Volumetric additive manufacturing (VAM) has emerged as a highly promising technology in advanced manufacturing, owing to its high production speed, excellent surface quality, minimal anisotropy, and the near absence of thermal and mechanical stresses during fabrication.[1-6] Despite these advantages, its broader implementation is hindered by a persistent process defect known as surface overcuring, which is the unintended crosslinking of resin in regions adjacent to the vat sidewalls.[7] Resin cured on the lateral vat walls can function as an additional optical lens, perturbing the propagation of projected light, while also acting as a physical obstruction to light penetration, thereby restricting subsequent polymerization predominantly to surface regions near the vat

sidewall.[8,9] As a result, surface overcuring can severely impair printing fidelity and, in extreme cases, cause complete failure of the printing process.

To mitigate this defect, a variety of strategies have been investigated. Several studies have adjusted ink formulations to minimize optical absorbance, ensuring that the light penetration depth exceeds the radius[10] or diameter[11,12] of the vat and thereby enabling effective polymerization in the intended region, although such modifications inherently restrict the range of usable materials. Behravesh *et al.*[7] further demonstrated that vat dimensions significantly affect surface overcuring: for parts with identical geometries and material systems, larger vat diameters are more likely to trigger this defect and lead to fabrication failure, whereas smaller vat diameters may help suppress it. Regarding the projection process, Madrid *et al.*[8] and Chen *et al.*[13] refined model-slicing strategies, which reduced light scattering and attenuation in turbid inks, thereby lowering the incidence of overcuring defects. These findings indicate that surface overcuring is governed by multiple factors, including material properties, hardware configuration, and light projection control. However, existing approaches remain largely case-specific and restricted to particular operating conditions. The evolution of surface overcuring under coupled multiphysical effects remains poorly understood. In addition, no universal printing process window is currently available to guide parameter selection. As a result, successful printing of three-dimensional (3D) structures, particularly in complex printing scenarios such as multilayered architectures fabricated with different materials,[9,14] still relies on empirical trial-and-error. This approach is not only inefficient and time-consuming, but also makes it difficult to identify optimal printing parameters.

The spatial distribution of light dose within the ink domain is a critical determinant of whether resin in the target region can be successfully cured during VAM. Mechanistically, the process is governed by the competition between accumulated light dose and oxygen inhibition, such that crosslinking polymerization proceeds only when the local accumulated light dose exceeds the curing threshold defined by oxygen depletion.[15-19] Ideally, for the *in situ* fabrication of 3D structures without surface overcuring, the accumulated dose within the target region should substantially exceed this threshold, whereas the dose near the boundaries should remain below it. In practice, however, the light-dose distribution within the dynamically rotating ink domain is governed by several interacting physical factors. The ink's intrinsic absorbance attenuates light along the optical path, thereby affecting energy delivery. Meanwhile, the geometric dimensions of the hardware, including the vat and occlusion, along with the projection domain, determine the propagation path of the projected light and, consequently, influence local dose accumulation. Rotational speed further modulates this accumulation process. The strong coupling among these factors makes precise control of light-dose distribution difficult to achieve through experimental trial-and-error alone. In this context, numerical simulation offers a powerful approach for resolving such multiphysics coupling problems, owing to its ability to quantify multivariable interactions and capture complex dynamic behavior.[20,21] Nevertheless, a theoretical model that can predict light-dose distribution while simultaneously accounting for these parameters remains unavailable. Establishing such a model would not only clarify the synergistic effects of multiple physical factors on light-dose distribution but also provide the basis for a generalized printing window to support the rational optimization and selection of practical process parameters.

In this study, we developed a theoretical model to analyze light-dose accumulation during the VAM process. By accounting for vat diameter, ink absorbance, and projection dimensions, the model enables the prediction of light-dose accumulation across different printing modes, including single-material and multi-material printing. The influence of these parameters on light-dose distribution was systematically examined, providing insight into the mechanism of surface overcuring. Based on this model, we further established a deterministic, multivariable printing process window that defines the safe operating boundaries for hardware design, material properties, and process parameters. To demonstrate the effectiveness and practical applicability of the proposed framework, we applied it to the fabrication of pH-responsive single- and multi-material drug delivery systems (DDSs) and subsequently performed functional validation.

2. Materials and methods

2.1. Materials

Poly(ethylene glycol) diacrylate (PEGDA, average MW 400 g/mol) was purchased from Shanghai D&B Biological Science Technology Co., Ltd. (China). Sodium alginate (SA), carboxymethyl chitosan (CMCS), and lithium phenyl(2,4,6-trimethylbenzoyl) phosphinate (LAP) were purchased from Shanghai Maclean Biochemical Technology Co., Ltd. (China). Metformin hydrochloride (MET) and bovine serum albumin (BSA) were obtained from Shanghai Aladdin Reagent Co. (China). All materials were used as received.

2.2. Preparation of printing ink

The LAP was employed as the photoinitiator and PEGDA as the photocrosslinker, while a CMCS/SA blend served as the polymer matrix for subsequent ionic crosslinking. To assess drug-release profiles, BSA (5% w/v) and MET (5% w/v) were incorporated as model macromolecular and small-molecule drugs, respectively, into the indicated formulations (pH-responsive [F1–F5] and non-responsive [F6]). It should be noted that a constant LAP concentration of 0.15% w/v was uniformly applied to all ink formulations in this study. This standardization was deliberately designed to eliminate the confounding effects of varying initiator concentrations on the photopolymerization kinetics, thereby ensuring a controlled investigation of the VAM process window. Ink preparation began by mixing PEGDA with deionized water, followed by the sequential addition of the model drug, LAP, SA, and CMCS under continuous magnetic stirring. The resulting hydrogel precursor was centrifuged at 2,000 rpm for 15 min for degassing. The detailed composition of each ink formulation is provided in Table 1.

2.3. Volumetric printing

2.3.1. Printing system

The computed axial lithography system comprises a projector (405 nm; PDC-03, GVINDA, China), a lens (21.0 × 19.0 f-19.00VIS, HYGX, China), and a monitoring camera (GP-1501, KCGP Instrument Co., Ltd., China) equipped with a red backlight source. The setup further included a transparent glass vat and a motor-driven rotating platform. The light patterns emitted by the projector were collimated to compensate for the radial distortion associated with the cylindrical vat, thereby ensuring precise projection into the center of the ink-filled vat. The vat was mounted on the rotating platform and rotated at a defined speed synchronized with the projection rate. A schematic representation of the printing system is provided in Figure 1A.

2.3.2. Printing process

All computer-aided design models used in this study were designed using SolidWorks (2021, Dassault Systèmes, France) and exported in STL format. The 3D geometries were then converted into a sequence of two-dimensional (2D) slices using the open-source VAM algorithm package developed by Kelly *et al.*,[10,15] from which the corresponding projection patterns were generated. These patterns were subsequently projected into the printing vat. The fabrication process was monitored in real time via a live camera feed to visually verify completion. Prior to projection, the vat was rotated for several minutes to ensure that the ink attained the same angular velocity as the vat, thereby preventing relative motion between the two. Upon completion of printing, the fabricated DDS was carefully retrieved and blotted dry to remove residual unpolymerized ink. The multi-material fabrication process began with the core unit, which was fabricated from the first type of ink (Ink A) using the previously described printing method. The fabricated core was then mounted on a custom-designed auxiliary fixture and transferred into a vat containing the second type of ink (Ink B). The VAM process was subsequently repeated to encapsulate the Ink A core within an outer shell formed by Ink B. This sequential strategy ultimately yielded the final multi-material construct.

2.4. Physicochemical characterization

2.4.1. Absorbance

The absorbance of all ink samples was measured at 405 nm using a ultraviolet–visible (UV–Vis) spectrophotometer

Table 1. Compositions of the ink

Formulation	SA (g)	CMCS (g)	LAP (g)	Drug (g)	PEGDA (mL)	Water (mL)
F1	1	0.5	0.15	5	5	95
F2	2	1	0.15	5	5	95
F3	2	1	0.15	5	10	90
F4	2	1	0.15	5	15	85
F5	4	2	0.15	5	5	95
F6	0	0	0.15	5	30	70

Abbreviations: CMCS: Carboxymethyl chitosan; LAP: Lithium phenyl(2,4,6-trimethylbenzoyl) phosphinate; PEGDA: Poly(ethylene glycol) diacrylate; SA: Sodium alginate.

(T2600, Youke Instrument Co., Ltd., China) with a 1 cm pathlength cuvette.

2.4.2. Drug photostability study

To assess whether the macromolecular model drug BSA and the small-molecule model drug MET undergo photodegradation during volumetric printing, their photostability was investigated. Separate test solutions of BSA and MET were first prepared at 20 μg/mL. The solutions were then placed in the vat of the VAM printer and exposed for varying durations (0, 5, 100, and 1000 s) under the same irradiation conditions used for DDS fabrication, including wavelength, projection pattern, and light intensity. Subsequently, the absorbance of the exposed solutions was determined using a UV–Vis spectrophotometer at 203 nm for BSA and 233 nm for MET, respectively.

2.4.3. Secondary crosslinking of the pH-responsive drug delivery system

The printed pH-responsive DDSs were subsequently subjected to a secondary ionic crosslinking treatment in a calcium ion solution to enhance their pH-responsive performance. Previous studies have demonstrated that excessively high calcium ion concentrations (>2%) or prolonged crosslinking times (>30 min) can significantly increase hydrogel crosslinking density, thereby impairing pH responsiveness.[22] Accordingly, in this study, the printed DDSs were post-treated in low-concentration calcium ion solutions (1% or 2% w/v) for 15 or 30 min, respectively, prior to swelling analysis.

2.4.4. Swelling rate

The printed DDSs were first snap-frozen for 2 h Subsequently, the frozen samples were immediately transferred to a freeze-dryer (12N/A, Scientz, China) and lyophilized for over 20 h at −80 °C under vacuum. The resulting lyophilized DDSs were weighed to determine the dry weight (W_0) before being immersed in either simulated gastric fluid (SGF; hydrochloric acid solution, pH 1.2) or simulated intestinal fluid (SIF; phosphate-buffered saline, pH 7.4) for swelling analysis. At predetermined time points, the DDSs were removed from the solution, and their wet weight (W_w) was recorded after gently blotting the surface with filter paper to remove excess solution. The swelling rate (SR) was calculated according to the following formula (**Equation 1**)[23]:

$$SR = \frac{W_W - W_0}{W_0} \quad (1)$$

2.4.5. Scanning electron microscopy

Scanning electron microscopy (MIRA3, Tescan, Czech Republic) was used to observe the microscopic morphology of the lyophilized printlet. The samples were cut with a thin blade, sputter-coated with gold, and then observed under a scanning electron microscope at 5 keV.

2.4.6. Fourier transform infrared spectroscopy

Infrared spectra of the products were obtained by scanning all samples at room temperature using a Fourier-transform infrared spectrometer (FTIR; Spectrum Two, Perkin-Elmer, USA). The scanning range was 2,000 cm^{-1} to 500 cm^{-1} with a resolution of 4.0 cm^{-1}.

2.4.7. In vitro drug release

The influence of DDS formulation and design on the drug release profile was evaluated with a dissolution apparatus (RCZ-12A, Yellow Sea Pharmaceutical Inspection, China). *In vitro* release was evaluated using the paddle method, operating at 100 rpm in 1,000 mL of SGF or SIF, with the temperature maintained at 37 °C. Aliquots of 10 mL were withdrawn at scheduled time points, and the absorbance was measured using a UV–Vis spectrophotometer. The cumulative drug release, calculated against a standard curve, was used to plot the release profiles. The dissolution study was performed in triplicate. The yielded first 60% drug release data were subsequently fitted to the Korsmeyer–Peppas model (**Equation 2**) for kinetic analysis:[24]

$$M_S / M_\infty = Ks^n \quad (2)$$

where s is the release time, M_s and M_∞ represent the cumulative drug release at time s and at equilibrium, respectively; K is a coefficient incorporating the structural and geometric characteristics of the drug-polymer system; n is the release exponent indicative of the drug transport mechanism. The value of n characterizes the release mechanism as follows: $n \leq 0.45$ corresponds to Fickian diffusion, $0.45 < n < 0.89$ suggests anomalous (non-Fickian) transport, and $n \geq 0.89$ indicates case-II transport, which is primarily governed by polymer relaxation or dissolution.[25]

2.4.8. Statistical analysis

All experimental data of this study are expressed as mean ± standard deviation or presented in the original data. In all experiments, each group had at least three samples. One-way analysis of variance was used to determine significant differences among multiple groups in the drug photostability study.

3. Results and discussion

3.1. Light dose distribution in the ink

To systematically investigate the light-dose distribution within the ink domain during VAM, a model was first developed to describe the spatial mapping relationship between the projection domain and the hardware configuration. Based on this model, the governing equations for light-dose accumulation within the ink were derived. Subsequently, a parametric study was conducted to assess the coupled influence of multiple physical factors on the resulting light-dose field.

3.1.1. Governing equations

Because overcuring is expected to occur first at the cross-section with the largest diameter of the 3D part, it is reasonable to investigate light-dose accumulation at this critical plane. Avoiding overcuring at the largest cross-section can effectively prevent it throughout the entire printed structure. Accordingly, the original 3D problem can be reduced to a 2D analysis. Figure 1B shows the geometric relationship between the hardware configuration of the printing system and the projection domain in the XY plane. The ink was contained within a cylindrical vat of inner radius R, which rotated uniformly about its central axis O at an angular velocity ω. A continuous projection beam of uniform intensity I_0 propagated along the optical axis from left to right and possessed a rectangular cross-section with a width of 2P. A cylindrical occlusion of radius z ($R > z \geq 0$) was positioned coaxially within the vat to partially occlude the beam, thereby simulating the shadowing effect of a pre-positioned structure on the light dose distribution during overprinting. It should be emphasized that in the established theoretical model, the cylindrical occlusion represents a pre-existing functional structure (e.g., a pre-printed core utilized in multi-material overprinting scenarios) that partially blocks the projection light, rather than the over-curing defect itself. Furthermore, surface overcuring is not treated as a predefined geometric entity. Instead, owing to the continuous rotation of the vat during the VAM process, severe surface overcuring results in an irregularly polymerized layer adhering to the inner wall. Both the projection domain and the vat were geometrically symmetric with respect to the optical axis. An arbitrary point B in the ink rotated together with the vat. From the onset of printing until time t, point B traversed an angle of θ, and its radial distance from O was denoted as r. Extending a horizontal auxiliary line leftward from B to intersect the vat boundary at point C, the segment BC defined the attenuation path length of the incident light reaching point B. For simplicity, the model was based on the following assumptions:

(i) The potential refraction at the resin–air (or vat) interface has been effectively compensated for by the designed collimating device.[10,13] With this boundary distortion neutralized, the attenuation of projected light within the ink strictly followed the Beer–Lambert law. Accordingly, secondary optical effects, such as scattering and internal reflection during propagation, were neglected, as their influence on the intensity distribution was considered minor compared to primary absorption.[15,16]

(ii) The occlusion was treated as an ideal, completely light-absorbing obstruction.[26] Thus, projected light could not penetrate it, and any potential refraction or reflection was disregarded.

(iii) Only the light-dose distribution corresponding to an integer number of complete vat rotations was considered, while cases involving incomplete rotations (e.g., half a revolution) were not included. This simplification is reasonable because, under ideal operating conditions, projection is expected to terminate only after the ink has completed an integer number of full rotations, thereby ensuring uniformity in both light-dose distribution and part geometry.[8]

(vi) The ink was regarded as an optically isotropic, homogeneous transparent medium, with no inhomogeneity in composition or density distribution.[15,26]

(iv) The projected beam dimensions were taken as the final printed part dimensions; shrinkage or expansion during or after printing was not accounted for in this model.[27]

The rotation period of the forming vat is defined as T. The light dose received at any point B within the ink over the interval [0, T] can be expressed as **Equation 3**:

$$E = \int_0^T I dt \tag{3}$$

where I denotes the projected light intensity at point B, with the light intensity in the ink decaying exponentially with the attenuation path length l, as explained by the Beer-Lambert law (**Equation 4**):

$$I = I_0 e^{\left(\frac{-l}{D_p}\right)} \tag{4}$$

where I_0 denotes the unattenuated light intensity, while D_p represents the optical penetration depth, a material-dependent parameter (**Equation 5**):

$$D_p = \frac{1}{\ln(10)A} \approx \frac{1}{2.3A} \tag{5}$$

where A is the absorbance of the material, measured using a 1 cm cuvette. The variable l is the attenuation distance of the projected light at point B within the ink, corresponding to the length of the line segment BC, as determined from the geometry (**Equation 6**):

$$l = \sqrt{R^2 - r^2 \sin^2 \theta} - r\cos\theta \tag{6}$$

Equation 6 captures the instantaneous change in exposure depth at ink point B during rotation, caused by the variation in its position relative to the light source. Here, R denotes the radius of the vat, r represents the distance from point B to the axis O, and θ signifies the central angle corresponding to the trajectory of point B from the initial moment to any arbitrary time t within the period $t \in [0,T]$. Then, it follows **Equation 7**:

$$\theta = \omega t \tag{7}$$

Combining **Equations 3** and **7**, the light dose E at any point within the ink can be expressed as **Equation 8**:

$$E = \frac{I_0}{\omega}\int_{\theta_1}^{\theta_2} e^{2.3A(-\sqrt{R^2-r^2\sin^2\theta}+r\cos\theta)}d\theta \tag{8}$$

where θ_1 and θ_2 are determined via geometric relationships. Depending on the presence ($z > 0$) or absence ($z = 0$ of an occlusion region, alongside the relative position between the ink and the projection zone, these geometric relationships can be categorized into four typical configurations, as illustrated in Figure 1C and 1D. The irradiated path of the point is indicated by a red arc. These four scenarios yield the following expression for the light dose accumulated at any point within the ink over one full rotation cycle:

$$E = \begin{cases} \frac{I_0}{w}\int_0^{2\pi} e^{2.3A(-\sqrt{R^2-r^2\sin^2\theta}+r\cos\theta)}d\theta, & z=0, r \int [0,P] \\ \frac{I_0}{w}\left[\int_{-\arcsin\left(\frac{P}{r}\right)}^{\arcsin\left(\frac{P}{r}\right)} e^{2.3A(-\sqrt{R^2-r^2\sin^2\theta}+r\cos\theta)}d\theta + \right. & \\ \left. \int_{\pi-\arcsin\left(\frac{P}{r}\right)}^{\pi+\arcsin\left(\frac{P}{r}\right)} e^{2.3A(-\sqrt{R^2-r^2\sin^2\theta}+r\cos\theta)}d\theta\right], & z=0, r \int (P,R] \\ \frac{I_0}{w}\int_{-\pi+\arcsin\left(\frac{z}{r}\right)}^{\pi-\arcsin\left(\frac{z}{r}\right)} e^{2.3A(-\sqrt{R^2-r^2\sin^2\theta}+r\cos\theta)}d\theta, & z>0, r \int [z,P] \\ \frac{I_0}{w}\left[\int_{-\arcsin\left(\frac{P}{r}\right)}^{\arcsin\left(\frac{P}{r}\right)} e^{2.3A(-\sqrt{R^2-r^2\sin^2\theta}+r\cos\theta)}d\theta + \right. & \\ \left. \int_{\pi-\arcsin\left(\frac{P}{r}\right)}^{\pi-\arcsin\left(\frac{z}{r}\right)} 2e^{2.3A(-\sqrt{R^2-r^2\sin^2\theta}+r\cos\theta)}d\theta\right], & z>0, r \int (P,R] \end{cases} \tag{9}$$

The derivation of **Equation 9** reformulates the light-dose evaluation from a time-dependent dynamic accumulation process into a radial-dependent, 2D path integral. This approach enables the static spatial quantification of light-dose distribution, thereby establishing a direct analytical link between material properties, hardware configurations, and process parameters. For clarity, all symbols and their corresponding definitions used in this study are summarized in Table 2.

Table 2. Definitions of the symbols used in this study

Symbols	Definitions
A	Absorbance of the in
D_p	Penetration depth
I	Projected light intensity at the point of interest
I_0	Incident light intensity
K	Coefficient incorporating the structural parameter of DDS
l	Attenuation path length
M_s	Cumulative drug release at time s
M_∞	Cumulative drug release at equilibrium
n	Release exponent indicative of the drug transport mechanism
P	Half-width of the projection beam
R	Inner radius of the forming vat
r	Radial distance of the point of interest from the center
s	Drug release time
T	Rotation period of the forming vat
t	Exposure time
W_0	Dry weight of the DDS
W_w	Wet weight of the DDS
z	Radius of the occlusion domain
θ	Angular position of the point of interest
ω	Angular velocity of the forming vat

Abbreviation: DDS: Drug delivery system.

3.1.2. Parametric study

Based on the derived equations, a parametric analysis was conducted to investigate the light-dose variations

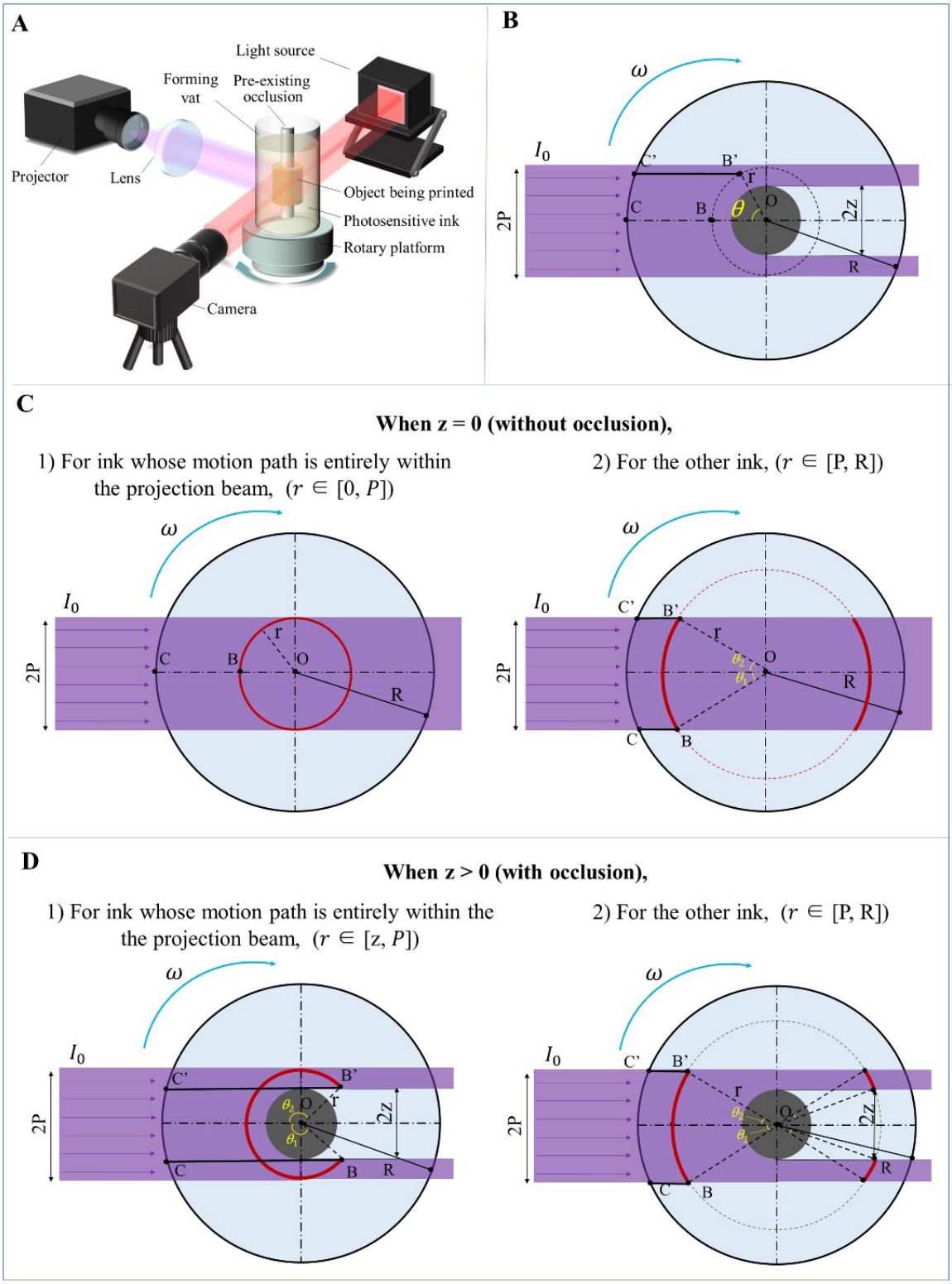

Figure 1. Schematic of the volumetric additive manufacturing system and the light-dose analysis model: (A) System configuration. (B) Two-dimensional model. Geometrical analysis of light-dose accumulation pathways for (C) $z = 0$ (without occlusion) and (D) $z > 0$ (with occlusion), respectively. P represents the half-width of the projection beam, r represents the radial distance of the point of interest from the center, and z represents the radius of the occlusion.

within the photosensitive ink under diverse conditions, as illustrated in Figure 2. Within the region $r \leq P$, the light dose E received by the ink increases with r at an accelerating rate. Consequently, the minimum printing dose invariably occurs at $r = 0$ in the absence of an occlusion, or at $r = z$ when an occlusion is present.

We first explored the impact of projection size P on light dose distribution in the ink domain. Figure 2A and 2B depicts the corresponding dose distributions for different values of P under a fixed hardware configuration and material absorptivity ($z = 0$ or $z > 0$, $R = 7.5$ mm, $A = I$). As P increases, the energy absorbed both at the ink surface E ($r = R$) and at the printing region edge E ($r = P$) increases, whereas the energy E ($r = 0$) or E ($r = z$) remains constant. This occurs because a larger projection size extends the effective exposure path for all points within the ink except at these specific positions, thereby increasing the integrated light dose E. Furthermore, the disparity in absorbed energy between the center and the edge of the printing region reflects its radial non-uniformity. Minimizing this gradient is therefore essential for preventing differential curing and maintaining dimensional fidelity.[28] Conversely, the energy differential between the printing core E ($r = 0$) or E ($r = z$) and the ink boundary E ($r = R$) characterizes the radial non-uniformity between the printing region and the ink surface. To effectively mitigate surface overcuring, it is imperative to maximize this differential, ensuring that the core dose, E ($r = 0$) or E ($r = z$), strictly exceeds the vat-boundary dose, E ($r = R$). As illustrated in Figure 2A, a suitable projection size (e.g., $P = R/3$) yields a higher dose at the center ($r = 0$) than at the surface ($r = R$). Under this condition, curing initiates preferentially within the target printing region, thereby effectively avoiding surface overcuring, as confirmed experimentally in Figure 2A. Conversely, when the projection size is enlarged (e.g., $P = R/2$), the light doses at the center and the surface become comparable. This induces concurrent curing in both regions, resulting in undesirable adhesion between the printed construct and the overcured surface layer, which ultimately causes severe geometric distortion, as evidenced in Figure 2A. At the other extreme, an excessively large projection size (e.g., $P = R/1.3$) reverses the dose distribution, concentrating energy primarily at the vat boundary. This leads to surface overcuring, which obstructs light transmission and suppresses subsequent curing in the target printing region, as shown in Figure 2A. Therefore, reducing the projection size not only concentrates the light dose within the target printing region, thereby mitigating surface overcuring, but also promotes more uniform curing and improves overall printing accuracy. While simple cylindrical models are sufficient for quantitatively identifying the overcuring boundary (as shown in Figure 2A), the destructive impact of this defect is profoundly magnified in complex geometries. As shown in Figure S1, severe surface overcuring can entirely obscure the intricate features of a target triply periodic minimal surface (TPMS) structure, resulting in an unrecognizable amorphous mass adhering to the vat wall, thereby highlighting the absolute necessity of operating within the established process window.

The impact of hardware configuration on light dose distribution in the ink domain was subsequently investigated. The light dose distributions for different vat radii R under a fixed projection size and material absorptivity ($P = 2.5$ mm, $A = 1$, $z = 0$) are shown in Figure 2C. As R increases, the difference between E ($r = P$) and E ($r = 0$) decreases, indicating a more uniform dose between the surface and center, consistent with the trend observed when reducing the projection size. However, this behavior simultaneously increases the light absorbed in the surface region, leading to a significant rise in E ($r = R$). This elevation is highly detrimental to volumetric printing, as it exacerbates the risk of surface overcuring. Specifically, for $R \leq 10$ mm, E ($r = 0$) is significantly larger than E ($r = R$); conversely, for $R \geq 15$ mm, E ($r = 0$) becomes notably smaller than E ($r = R$). In the other cases, the light dose levels at the center of the printing region and vat boundary are comparable. This occurs because, for a fixed projection size, a larger R results in a longer attenuation path within the ink. Consequently, more light energy is absorbed in the non-printing region, which reduces the magnitude of the light dose delivered to the printing region. Therefore, reducing the vat size helps suppress surface overcuring, a trend consistent with the findings of Behravesh *et al.*[7] Maintaining constant vat dimensions, projection size, and material properties ($R = 7.5$ mm, $P = R/3$, $A = 1$), the size of the occlusion region z was systematically varied. The resulting light dose distribution is shown in Figure 2D. As z decreases, the light dose at the vat boundary, E ($r = R$), remains invariant, whereas the dose at the occlusion boundary, E ($r = z$), diminishes significantly. This variation increases the risk of surface ink overcuring. Therefore, increasing the size of the occlusion region helps mitigate surface overcuring.

A similar analysis was also conducted for material absorbance, as illustrated in Figure 2E and 2F, which shows the spatial light-dose distribution within the resin across varying absorbance values. It can be observed that when $z > 0$, the light dose E within the ink is noticeably lower than that in the $z = 0$ case, and the difference between the center and the edge of the printing region is also significantly larger. This occurs because the occlusion region obstructs the propagation of the projected light,

reducing the accumulation of light energy within the ink and intensifying the unevenness of its distribution. Furthermore, as the material absorbance A increases, the light dose received in the central region decreases significantly, while that at the surface region is only slightly reduced. This pronounced disparity makes suppression of surface overcuring particularly challenging in VAM systems. Specifically, when $A < 1$, $E\ (r = 0)$ is significantly larger than $E\ (r = R)$; when $A \geq 2$, $E\ (r = 0)$ becomes notably smaller than $E\ (r = R)$. In other cases, the light dose levels at these two regions are roughly comparable. This trend occurs because ink with higher absorbance attenuates more light and reduces penetration, thereby confining more light energy to the surface, which readily leads to overcuring. This observation is consistent with the findings reported in Xie *et al.*[9] Therefore, under otherwise fixed process parameters, reducing the material absorbance helps prevent overcuring defects in the surface region.

Synthesizing the preceding parametric analysis, it becomes evident that increases in ink absorbance, projection size, and vat dimensions, alongside a reduction in the occlusion region size, collectively drive the light dose towards the periphery of the ink domain, thereby exacerbating the risk of surface overcuring defects. Therefore, the spatial distribution of the light dose is governed by the spatial coupling of these physical factors, rather than by any single parameter. The adverse impacts induced by highly absorbent inks can thus be offset by reducing the vat radius or projection size. Given that these multidimensional parameters collectively govern the final energy field distribution, conventional empirical optimization based on trial-and-error for individual variables[7,9,14] fails to capture the complex dependencies inherent in this system. Such approaches struggle to establish a reliable operating space to circumvent surface overcuring. Therefore, achieving stable, predictable volumetric fabrication necessitates integrating these coupled parameters into a comprehensive printing process window, thereby quantitatively defining their safe operating boundaries.

3.2. Printing process window

The light-dose field analysis presented in Section 3.1 reveals that surface overcuring can be prevented when the light dose in the target printing region exceeds that at the ink periphery. Accordingly, this section establishes a coupled multivariable printing process window based on this criterion. The validity of this operating window was subsequently evaluated through printing experiments and literature data. The results indicate that parameter sets falling within these boundaries effectively suppress surface overcuring, thereby providing a rational basis for the fabrication of the DDSs described in the subsequent sections. To mathematically formalize this criterion, the critical condition is defined piecewise according to whether an optical occlusion is present, as shown in **Equation 10**:

$$\begin{cases} E(r=0) > E(r=R), z=0 \\ E(r=z) > E(r=R), z>0 \end{cases} \tag{10}$$

By substituting the analytical light-dose expressions (**Equation 9**) into **Equation 10**, the expanded inequalities defining the process window are derived as **Equation 11**:

$$\begin{cases} \pi e^{(-2.3AR)} > \int_0^{\arcsin\left(\frac{P}{R}\right)} \left(1+e^{(-4.6AR\cos\theta)}\right) d\theta, & z=0 \\ \int_0^{\frac{\pi}{2}} e^{2.3A\left(-\sqrt{R^2-z^2\sin^2\theta}+z\cos\theta\right)} d\theta > \arcsin\left(\frac{P}{R}\right) & \\ +\int_{\arcsin\left(\frac{z}{R}\right)}^{\arcsin\left(\frac{P}{R}\right)} e^{(-4.6AR\cos\theta)} d\theta, & z>0 \end{cases} \tag{11}$$

Equation 11 defines the printing process window that prevents surface overcuring. The equation incorporates three variable groups: the projection size (P), the material absorbance (A), and the hardware configuration parameters (R and z). By assigning fixed values to any single variable group, a 2D printing window delineated by the remaining two parameter groups can be derived. Consequently, to provide concrete guidance for the practical application in subsequent chapters, the specific hardware parameters of the printing system utilized in this study (R = 7.5 mm, z = 0 or $z = R/3$) were substituted into the equation. This yields a system-specific 2D printing process window bounded by the material and printing parameters, as shown in Figure 3A.

As illustrated in Figure 3A, the red region indicates the theoretical operating window where surface overcuring could be effectively suppressed without occlusion (z = 0), whereas the blue region denotes the window when an occlusion with a radius of $R/3$ ($z = R/3$) is present. For practical applications, printing parameters must be selected within these defined regions to avert surface overcuring. The validity of this theoretical window was empirically corroborated: parameters yielding successful (solid circles) and failed (solid triangles) outcomes align with the predicted boundaries; points outside the window result in overcuring and wall adhesion, whilst those inside ensure successful fabrication. Furthermore, this process window is supported by successful printing parameters extracted from extensive literature,[2,7–9,12,13,27,29] which are characterized by an absence of surface overcuring (Table S1). Parameters within the defined windows enable the fabrication of

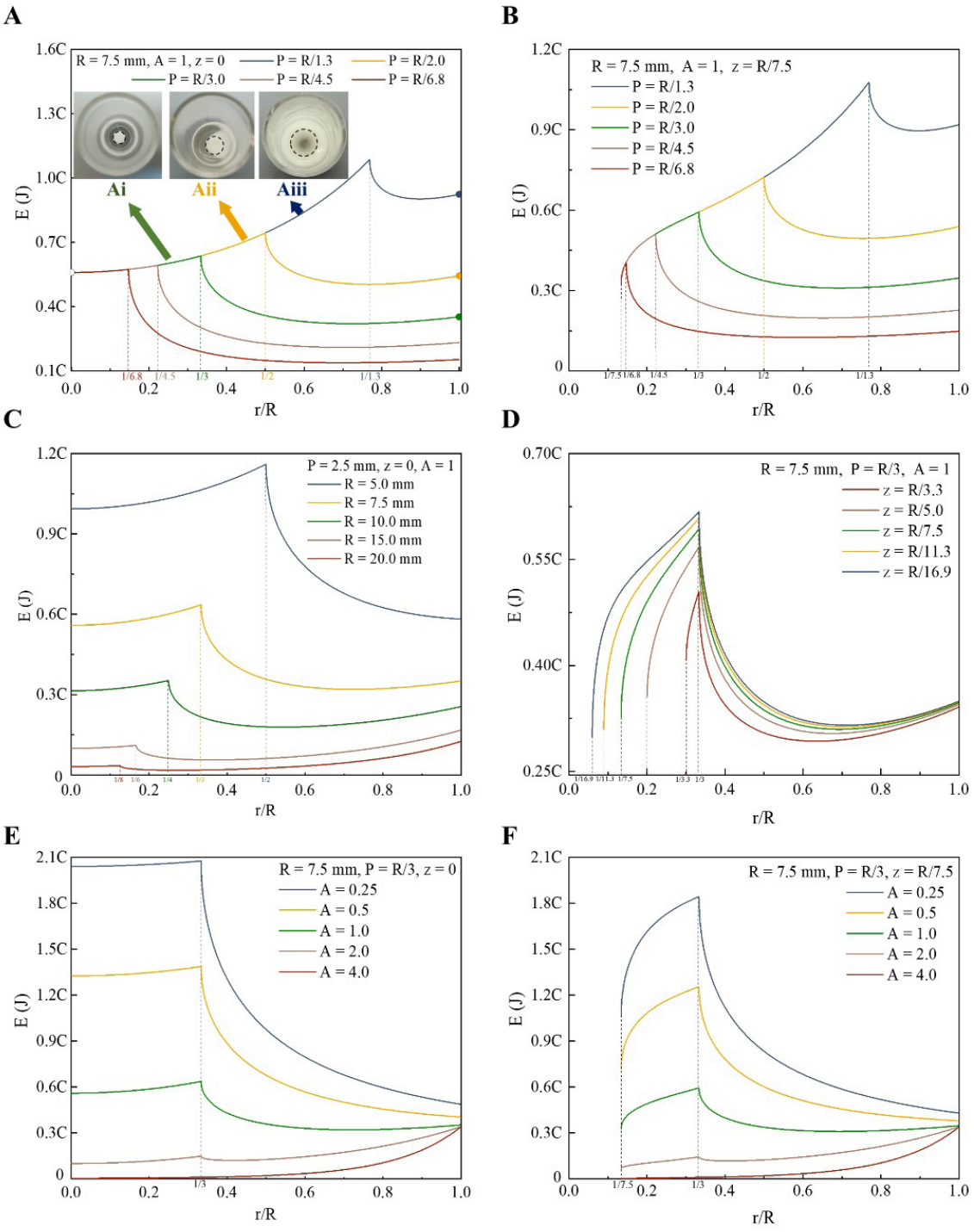

Figure 2. Parametric investigation of light-dose distribution within the ink. Influence of the projection size P at (A) $z = 0$ and (B) $z > 0$, respectively. Ai, Aii, and Aiii show the actual printing results corresponding to $P = R/3$, $P = R/2$, and $P = R/1.3$, respectively. The intended boundaries of the target constructs and the undesired overcured resin are delineated by black dashed outlines (enlarged views of these insets are provided in Figure S2). (C) Influence of the forming vat's radius R. (D) Influence of the occlusion domain's radial size z. Influence of ink absorbance A at (E) $z = 0$ and (F) $z > 0$, respectively.
Note: The Y-axis is scaled by the constant C, where $C = I_0/\omega$. Since the occlusion occupies the region $r \leq z$, the light-dose field within the ink is not considered in this region in the presence of an occlusion.

complex geometries, including hollow structures and overhangs, without surface overcuring (Figure 3B and 3C). To experimentally validate the reliability and practical effectiveness of the established printing process window, representative 3D models, including TPMS, The Thinker, and body-centered cubic (BCC), were fabricated. As shown in the multi-angle photographs (Figure S3) and the corresponding dimensional measurements (Table S2), these intricate features were formed with complete structural integrity. These quantitative and visual results convincingly demonstrate that the proposed physics-based process window effectively guides the VAM fabrication process, ensuring the successful construction of these complex targets while preventing severe overcuring and printing failures. This printability can be attributed to the lower light dose required to form complex geometries compared to solid cylinders of equivalent dimensions. This likely reduces their susceptibility to overcuring, thereby accounting for their successful fabrication within the established process windows.

Previous studies have largely neglected the coupled influences of process conditions, hardware configuration, and material properties, instead relying on constraining ink composition such that absorbance remains below a fixed threshold (e.g., $A \leq 0.58$[10] or $A \leq 0.29$[11,12] for the hardware used in this work) to suppress overcuring. However, these static strategies cannot readily accommodate variations in practical operating conditions, thereby limiting both the scalability of process parameters and the potential for performance optimization. By contrast, the present study establishes a coupled, multivariable, dynamic printing window that defines the acceptable absorbance range for target inks under specific printing conditions. This method not only broadens the feasible parameter space and enhances part performance but also provides a technical basis for the quantitative design and controlled manufacturing of complex structures via VAM.

To investigate the influence of hardware parameters on the process window, the effect of vat size R was first evaluated with the occlusion size fixed ($z = 0$ or $z = R/3$), as shown in Figure 4A and 4B. The results indicate that, for a given print size, the permissible upper limit of the material's absorbance decreases as the vat size R increases, regardless of occlusion. A similar decrease occurs with an increase in the relative projection size (P). This trend results from the enlargement of the vat and the projection size, which shifts more light energy toward the peripheral regions of the ink, thereby increasing the risk of overcuring. Appropriately reducing the material's absorbance can counterbalance this effect. Additionally, it was observed that under identical hardware configurations, higher material absorbance limits the maximum printable radial dimension, a constraint further exacerbated by occlusions. Consequently, the overprinting mode in VAM, used for fabricating multi-material components,[30,31] exhibits a higher susceptibility to surface overcuring compared to the direct printing mode. Therefore, to maximize the available radial design space, high-absorbance materials should ideally be allocated to the inner core, with low-absorbance materials forming the outer shell. This strategic arrangement effectively broadens the geometric window for complex multi-material structures. Figure 4C illustrates the impact of varying the occlusion size (z) on the printing window while maintaining other parameters constant. At a fixed projection size, a smaller z requires a lower allowable absorbance threshold to achieve successful volumetric printing. The underlying reason is that reducing z allows the ink to occupy more of the central, optically unfavorable zone, where the light dose E ($r = z$) is inherently lower due to longer attenuation paths. Consequently, to ensure the curing of the target region, the material's absorbance upper threshold is reduced.

In summary, establishing this coupled multivariable process window shifts the VAM manufacturing paradigm from empirical trial-and-error to deterministic quantitative control. The results show that the printing boundary should not be regarded as a static threshold, but rather as a dynamic limit governed by the interplay between material optical properties and the geometric constraints of the printing system. This theoretical framework not only guides the selection of practical printing parameters but also provides a rigorous basis for mitigating surface overcuring in real manufacturing environments. In engineering practice, low-absorbance materials have generally been employed to prevent surface overcuring,[9-12] whereas highly absorbent inks often result in fabrication failure, thereby substantially restricting the range of materials applicable to VAM. In contrast, the dynamic process window established in this study demonstrates that surface overcuring can be circumvented by adjusting hardware configurations or the geometric dimensions of the target construct, without requiring changes to the ink formulation. This insight is of considerable engineering importance because it relaxes the traditional constraints placed on material optical properties, avoids the need to compromise formulation design, and extends the applicability of VAM to high-absorbance material systems.

It should be emphasized that VAM inherently involves the coupling of complex physical processes and nonlinear photopolymerization chemistry. Compared with recently reported models that incorporate nonlinear photopolymerization kinetics,[32,33] the model developed

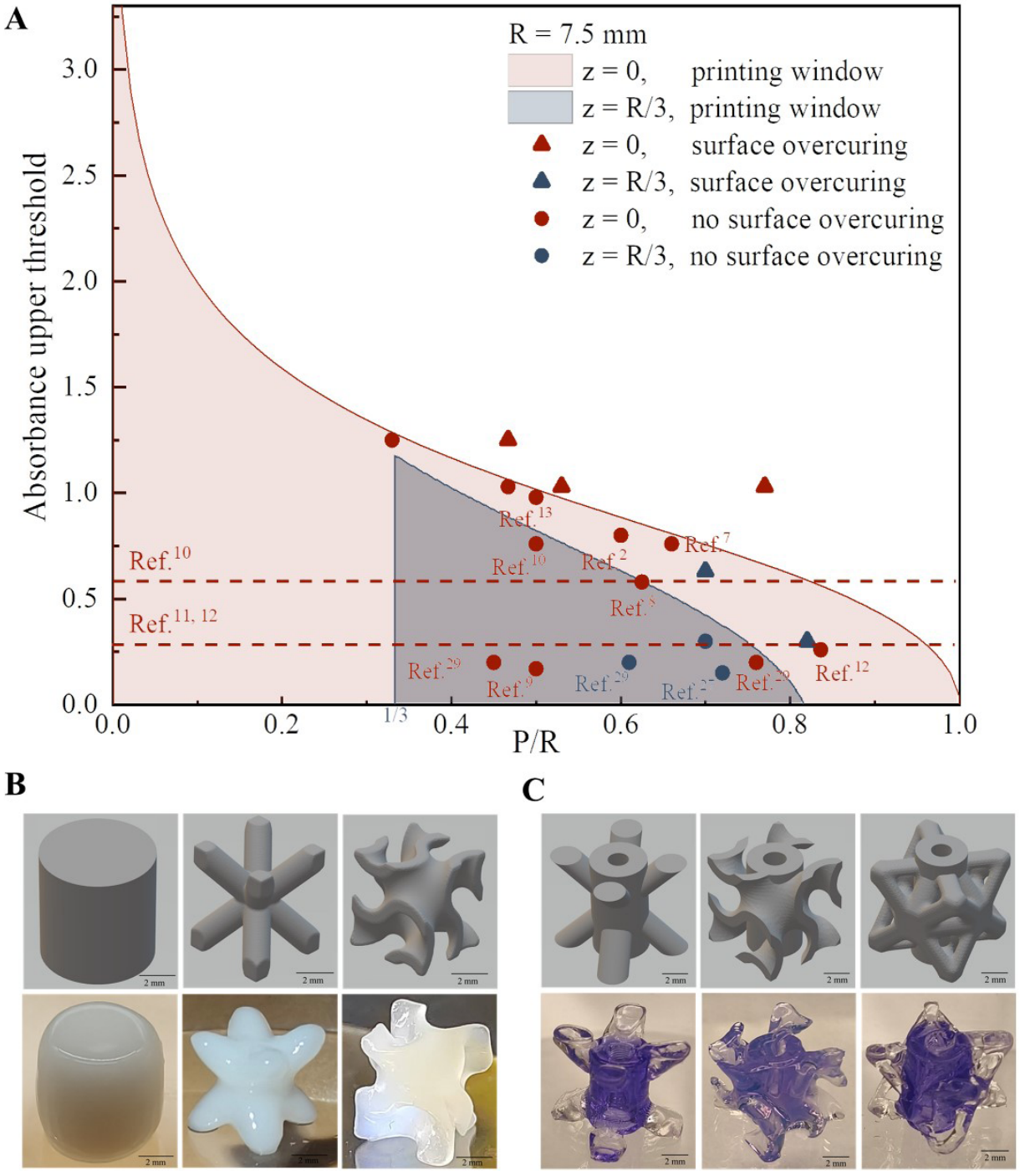

Figure 3. Theoretical printing process window and its experimental validation. (A) Printing process window for preventing surface overcuring compatible with the hardware configuration used in this study. The red region indicates the theoretical operating window where surface overcuring can be effectively suppressed without occlusion, whereas the blue region denotes the window when an occlusion with a radius of $R/3$ is present. Representative prints of complex geometries fabricated under the guidance of the process window: (B) for $z = 0$ (printing parameters: $A \approx 0$, $R \approx 7.5$ mm, $r \approx 3.5$ mm); (C) for $z = R/3$ (printing parameters: $A \approx 0.3$, $R \approx 7.5$ mm, $r \approx 5$ mm). Specifically, a transparent material was used to print the outer shell structure, whereas the inner core structure was dyed with gentian violet to provide visual distinction. P represents the half-width of the projection beam, r represents the radial distance of the point of interest from the center, and z represents the radius of the occlusion.

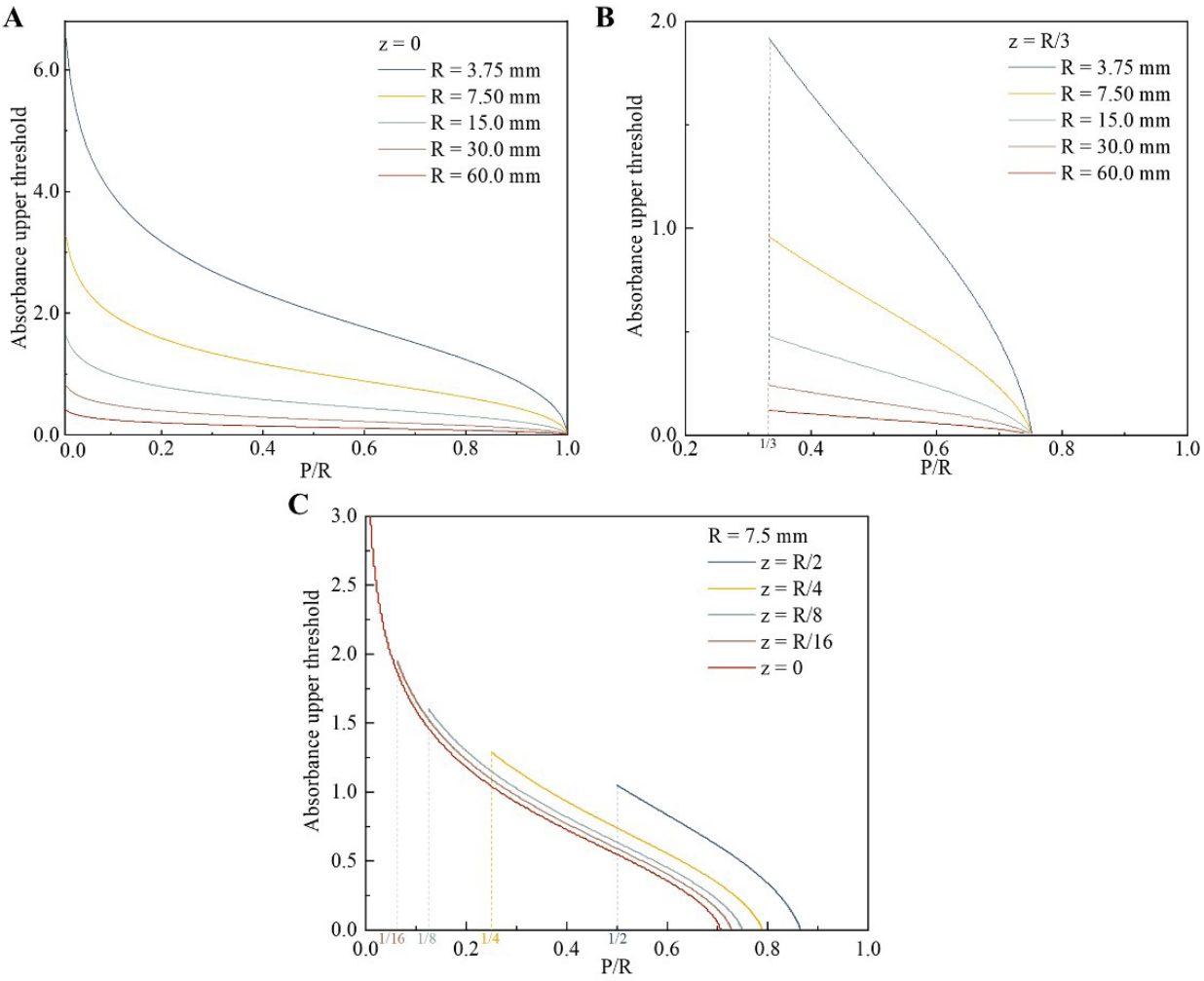

Figure 4. Influence of hardware parameters on the printing process window (bounded by the projection beam size and the upper absorbance threshold of the ink). Influence of vat radius *R* on the window at (A) $z = 0$ and (B) $z > 0$, respectively. (C) Influence of the occlusion radius *z* on the window. *P* represents the half-width of the projection beam, *r* represents the radial distance of the point of interest from the center, and *z* represents the radius of the occlusion. Note: Since the occlusion occupies the region $r \leq z$, the printing process window is not considered in this region in the presence of an occlusion.

in this study primarily accounts for spatial accumulation of light dose and does not consider reaction–diffusion behavior of the photosensitive ink. As a result, it cannot accurately predict structural deformation and other complex curing behaviors arising from local variations in reaction and diffusion rates as more advanced models do.[32,33] Nonetheless, the dose-based framework established here remains useful for macroscopic analysis of how multiple process parameters collectively affect the light-dose distribution, allowing the identification of an effective process window and the suppression of surface overcuring by regulating the dose gradient. In addition, this model offers relatively high computational efficiency. Incorporating photopolymerization kinetics into the present framework will therefore be an important direction for future work, with the aim of improving predictive accuracy and better capturing localized curing behavior.

3.3. Single-material drug delivery system fabricated via volumetric additive manufacturing

This section presents the optimal design and fabrication of a pH-responsive DDS by VAM. pH-responsive DDSs enable stimuli-triggered drug release within specific physiological environments, such as the pH gradient of the gastrointestinal tract.[34] SA and CMCS are utilized for constructing these systems owing to their biocompatibility, pH-responsiveness, and aqueous solubility.[35-37] This solubility facilitates premixing with photosensitive materials, such as PEGDA, to formulate a composite

ink for VAM. Through sequential photopolymerization and ionic crosslinking, the composite ink forms an interpenetrating network structure, imparting pH-responsive and passive targeting capabilities to the DDS.[38-40] It should be emphasized that the optimization of drug release performance is intrinsically governed by the parameters of the established printing process window. The functional inks required for these systems possess relatively high light absorbance (up to 1.23, as detailed in Section 3.3.1) and are therefore highly susceptible to severe surface overcuring.[7-13] Consequently, the process window not only serves as the fundamental technical prerequisite for their successful fabrication, but also directly dictates their maximum printable geometric dimensions. Since drug release kinetics are highly dependent on the carrier's macroscopic geometry and surface area, the structural design for optimizing release profiles must be strictly executed within the parametric boundaries defined by this printing window. Guided by these established boundaries, the swelling behavior and drug-release performance of the printed DDSs were then systematically evaluated to identify the formulation that provides the optimal pH-responsive behavior.

3.3.1. Geometric design

Figure 5A illustrates the preparation process and the corresponding drug release mechanism. To identify the optimal pH-responsive ink formulation, standardization of the printed DDS geometry is required for parallel comparisons. Because the maximum printable radius of an ink is constrained by the hardware design and the material absorbance, the DDS geometry must be designed within the applicable printing window. Based on the findings in Section 3.2, the printing process window for the specific hardware configuration ($z = 0$, $R = 7.5$ mm) was first delineated. The absorbance of five candidate pH-responsive inks (F1–F5) was measured, and the maximum printable radius for each was derived, as depicted in Figure 5B. Among these, ink F5 exhibited the highest absorbance (~1.23), which dictated a maximum printable radius of approximately 2.7 mm. Consequently, for parallel comparison, all DDSs were uniformly printed as cylindrical structures with a radius of 2.5 mm and a height of 8 mm for subsequent swelling and drug release studies.

3.3.2. Optimization of the swelling behavior

The drug release properties of hydrogels are linked to their swelling behavior. During swelling, increased water content enhances polymer chain mobility and expands the free volume available for diffusion, influencing release kinetics.[41] Consequently, the swelling capacity of the printed DDS modulates the mechanism and kinetics of active drug release.[42] Post-processing is required to achieve pH responsiveness in the DDS. During this stage, ionic chelation between carboxyl groups and divalent cations (e.g., calcium ion) forms a network. This crosslinked structure dictates the swelling behavior and subsequent drug release profile under varying pH environments.[43] To minimize bias from boundary variables and enhance the generalizability of the post-processing protocol, formulation F3 was selected as a representative formulation for parameter optimization. Situated at the center of the formulation parameter space, F3 balances an intermediate loading of pH-responsive components (3.0 g CMCS and SA) with a moderate crosslinking density (10 mL PEGDA). This ensures that the post-processing parameters derived from F3 can be effectively generalized across other formulations with varying polymer concentrations. Figure 5C presents the SR profiles for DDSs treated under various conditions in SGF (pH 1.2) and SIF (pH 7.4), while Figure 5D illustrates the corresponding SR statistics. The results indicate that most DDSs reached swelling equilibrium within approximately six hours under all tested conditions. Among them, the DDS treated with 2% calcium chloride solution for 15 minutes achieved the highest SR differential (1.22) between pH 7.4 and pH 1.2, demonstrating pH responsiveness. This protocol provides a basis for achieving site-specific drug release and was adopted for all subsequent DDS fabrication.

To screen for the optimal pH-responsive ink, the equilibrium swelling behavior of DDSs with varying compositions was evaluated. Figure 5E shows that the majority of the DDS reached swelling equilibrium within approximately six hours. Furthermore, the ratio of the equilibrium SR in SIF to that in SGF was determined to quantify the pH-responsiveness, as shown in Figure 5F. A trend emerged where the SR in both media increased concomitantly with decreasing PEGDA content. This phenomenon is attributed to the fact that reducing the monomer concentration lowers the crosslinking density of the polymeric network, yielding a more porous and swellable architecture. Formulations F1, F2, and F5 exhibited pH-responsive swelling, as their equilibrium SR values in SIF were 1.26, 1.31, and 1.55 times higher than those recorded in SGF, respectively. Furthermore, increasing the SA/CMCS concentration was found to reduce SR in acidic environments while enhancing it in alkaline environments, resulting in greater pH responsiveness. This behavior stems from the pH-dependent ionization of the carboxyl groups inherent to SA and CMCS. Specifically, higher polymer concentrations under acidic conditions lead to extensive protonation, which suppresses the network's charge density and hydrophilicity, thereby driving structural contraction.[44] This mechanism was subsequently validated

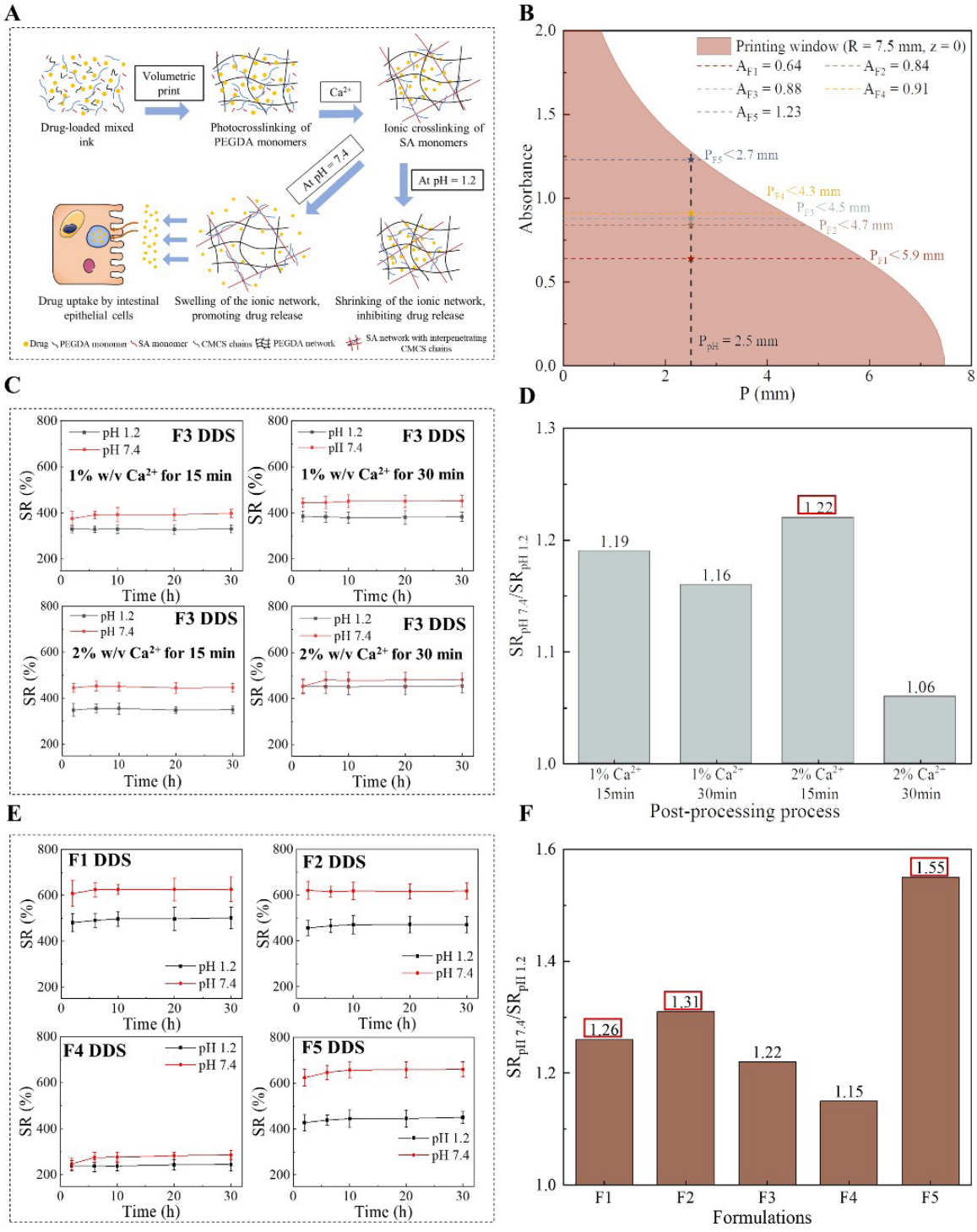

Figure 5. Design and swelling characterization of pH-responsive DDS. (A) Schematic of the pH-responsive DDS illustrating its fabrication process and drug release mechanism. (B) Printing window derived based on the hardware parameters (R = 7.5 mm, z = 0). (C) Temporal SR profiles under varied post-processing conditions. (D) Corresponding ratio of equilibrium SR between SIF and SGF. (E) Temporal SR profiles of different formulations (F1–F5). (F) Corresponding ratio of equilibrium SR (SIF/SGF) for each formulation.

Abbreviations: CMCS: Carboxymethyl chitosan; DDS: Drug delivery system; PEGDA: Poly(ethylene glycol) diacrylate; SA: Sodium alginate; SGF: Simulated gastric fluid (pH 1.2); SIF: Simulated intestinal fluid (pH 7.4); SR: Swelling ratio.

through morphological observations via scanning electron microscopy.

3.3.3. Drug release behavior

The FTIR spectra in Figure 6A confirm the integration of components into the printed DDS, with no structural alteration of the model drug BSA. Characteristic peaks at 1,720 cm^{-1} (C=O) and 810 cm^{-1} (C=C) from PEGDA are present. The decrease in intensity of the C=C peak indicates its consumption during photopolymerization to form C–C bonds.[45] Peaks around 1,405 cm^{-1} correspond to carboxyl groups of CMCS/SA, while those near 1,650 cm^{-1} are attributed to amide bonds in BSA. The absence of a shift in the BSA amide peaks suggests that its secondary structure remained intact, with no chemical interactions among components during printing. Subsequently, the stability of two model drugs, BSA and MET, was examined under varying irradiation durations. As shown in Figure 6B and 6C, no difference in drug content was observed between the control (no irradiation) and groups irradiated for 5, 100, or 1,000 s. These results confirm that, under the employed printing conditions, ultraviolet exposure does not cause photodegradation of these drugs.

Based on the swelling results, three ink formulations (F1, F2, and F5) characterized by pH-responsive properties and increasing total SA/CMCS concentrations were selected for *in vitro* drug release studies (Figure 6D, 6G, and 6J). The release rate of the model drug was higher in SIF (pH 7.4) than in SGF (pH 1.2). This differential became more apparent with increasing SA/CMCS concentration, reflecting pH-responsive behavior that aligns with the swelling trend. This correlation occurs because hydrogel swelling increases the effective surface area for drug diffusion, promoting release. Among the tested formulations, the F5 DDS showed the highest pH responsiveness, with drug release ratios (SIF vs. SGF) of 2.4 at 2 h and 1.7 at 48 h. These findings suggest that the F5 formulation is a candidate for colon-targeted delivery of protein-based therapeutics. To elucidate the drug release mechanisms, the release profiles were fitted to the Korsmeyer-Peppas model. The release exponent n for all formulations was less than 0.45, indicating that drug release followed a Fickian diffusion mechanism. The microscopic morphology associated with release behavior differs with pH. In SIF, higher polymer concentrations increase network hydrophilicity and swelling capacity, resulting in a porous structure (Figure 6E, 6H, and 6K).[41,42] This reduces resistance to drug diffusion but increases the time for polymer chain disentanglement and rearrangement during hydration (the swelling–relaxation process). In contrast, increased SA and CMCS concentrations in SGF lead to protonation-induced network contraction, forming a compact physical barrier (Figure 6F, 6I, and 6L).[34,42] In this acidic environment, the drug diffusion path becomes tortuous, decreasing the effective diffusion coefficient.

In conclusion, the established VAM process window enabled the determination of printable geometries and the successful fabrication of functional DDSs using highly absorbent inks. Analysis of the drug-release kinetics identified formulation F5 as the most suitable drug-delivery carrier owing to its strong pH-responsive behavior. These results confirm the reliability of the single-material printing process window and establish the parametric and material basis for the subsequent development of multi-material DDSs.

3.4. Multi-material DDS fabricated via volumetric additive manufacturing

Building upon the printing process window established in Section 3.2 and the optimal pH-responsive ink formulation identified in Section 3.3, this section presents the design and fabrication of multi-material DDSs via VAM. These systems enable the simultaneous loading of multiple drugs with controlled release profiles. This capability facilitates therapy for patients with comorbidities, such as peptic ulcers and diabetes, and simplifies complex dosing regimens.[46] To fabricate such multi-material DDSs, an overprinting strategy and the geometric design of the multi-material structures are first detailed, followed by an evaluation of the multi-drug release kinetics.

3.4.1. Geometric design

In VAM, directly fabricating multi-material structures within the ink domain in the absence of external auxiliary support is constrained by the stability of the components.[47] Fabricated components suspended within the ink domain are affected by external perturbations and spatial displacements. This spatial instability affects the direct overprinting of these structures with new encapsulating material. To address this, this study deployed pre-positioned auxiliary support structures within the printing vat to fix the fabricated components, preventing displacement during the subsequent printing process.[48,49] A schematic of the printing process is shown in Figure 7A.

Based on Section 3.2, placing high-absorbance material in the inner layer yields a broader printing window. Therefore, the pH-responsive F5 ink was selected for the core, while the low-absorbance, non-pH-responsive F6 ink was employed for the shell. The inner core is printed under unobstructed conditions. Referring to the printing window in Figure 5B (R = 7.5 mm, z = 0), the core is designed as a ring shape with an outer radius of 2.5 mm to facilitate installation. During overprinting of the shell, the pre-

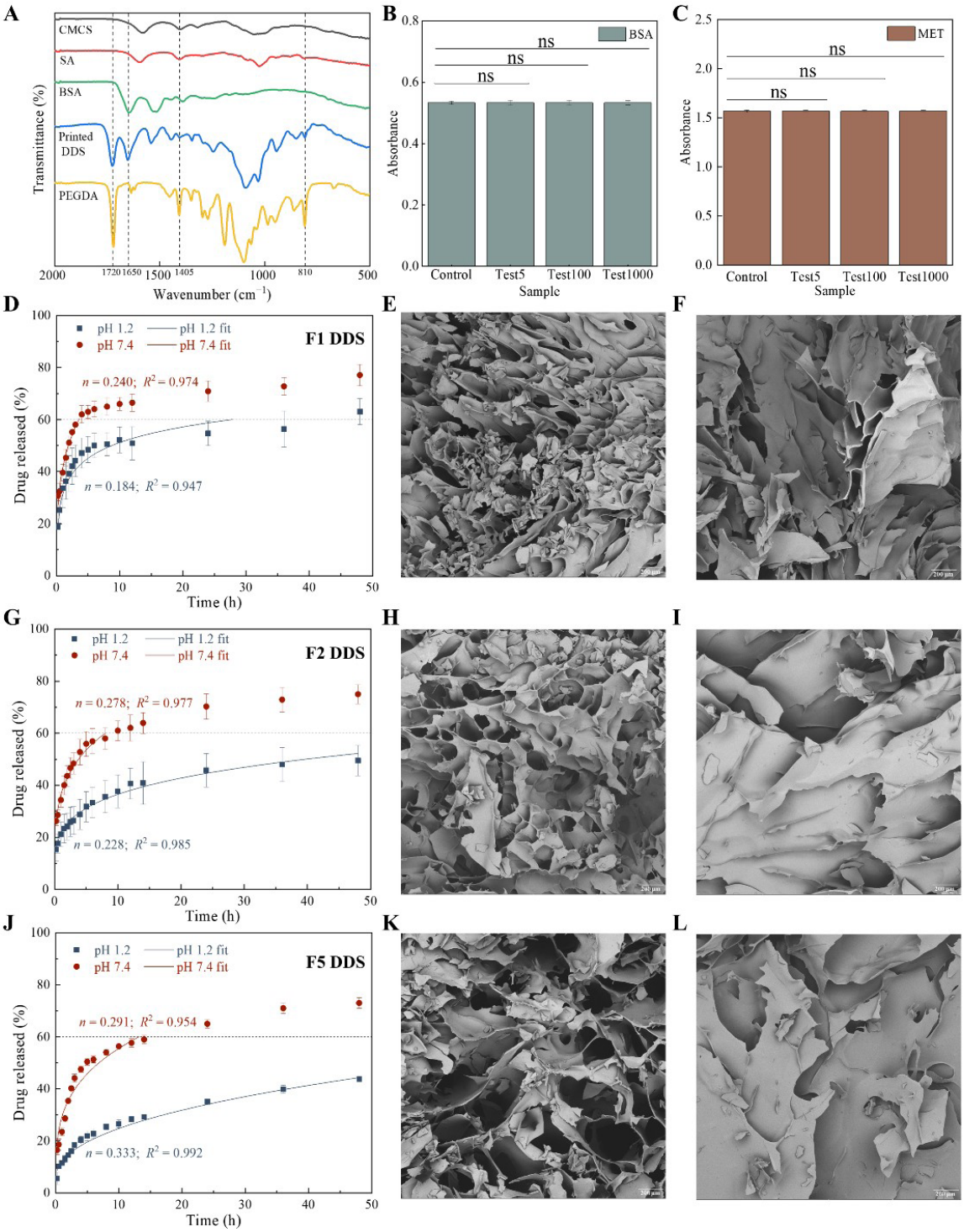

Figure 6. Characterization and drug release analysis of the pH-responsive DDS. (A) Fourier transform infrared spectroscopy spectra of the ink raw materials and the printed DDS. Photostability test results of the (B) model drugs BSA and (C) MET, respectively. Drug release profiles of DDS formulations (D) F1, (G) F2, and (J) F5, respectively. Internal cross-sectional microstructures of DDS formulations (E) F1, (H) F2, and (K) F5 after drug release in SIF (pH 7.4). Internal cross-sectional microstructures of DDS formulations (F) F1, (I) F2, and (L) F5 following drug release in SGF (pH 1.2).

Abbreviations: BSA: Bovine serum albumin; CMCS: Carboxymethyl chitosan; DDS: Drug delivery system; MET: Metformin hydrochloride; ns: Not significant; PEGDA: Poly(ethylene glycol) diacrylate; SA: Sodium alginate.

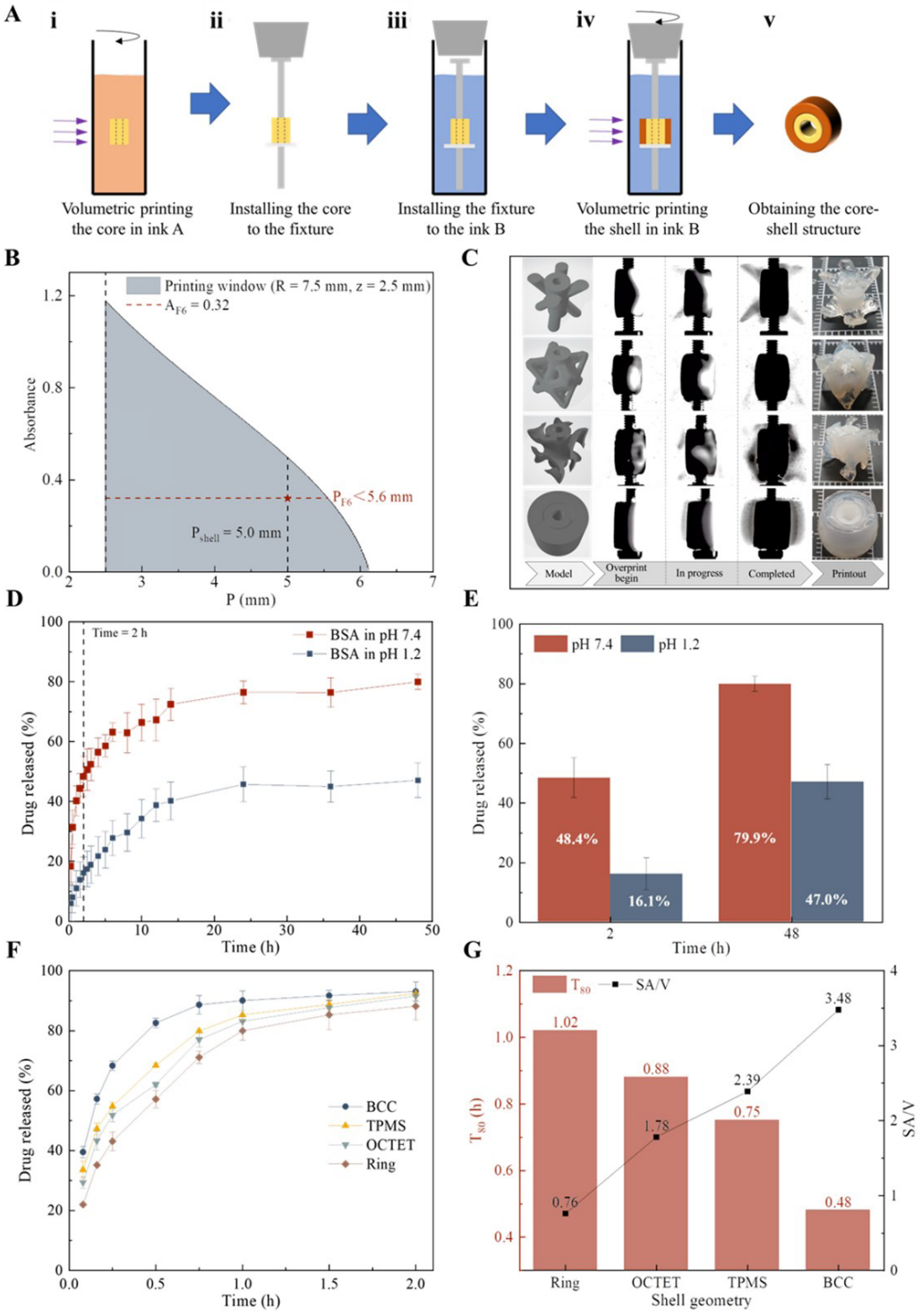

Figure 7. Printing methods, processing windows, and drug release analysis of multi-material DDS. (A) Schematic of the volumetric printing strategy for multi-material structures. (B) Printing window derived using the hardware parameters (R = 7.5 mm, z = 2.5 mm). (C) Design model, *in situ* monitoring images during the overprinting process, and photographs of the final multi-material constructs. (D) Drug release curves of the pH-responsive core structures and (E) the corresponding cumulative release analysis. (F) Drug release profiles of different non-responsive shell structures and (G) the corresponding comparative analysis of their release behavior.

Abbreviations: BCC: Body-centered cubic; OCTET: Octet truss; SA/V: Surface area-to-volume ratio; TPMS: Triply periodic minimal surface.

positioned core structure acts as an obstruction (z = 2.5 mm) that shields portions of the optical path, altering the cumulative dose distribution. Crucially, this obstruction can be treated effectively as a light-blocking zone due to its strong optical attenuation. Optical measurements (Figure S4) confirm that the cured F5 hydrogel exhibits an apparent absorbance reaching the instrumental limit ($A \geq 10$ at a 10 mm path length), meaning over 90% of light energy is dissipated per millimeter of penetration. Geometric analysis of the printed core (outer radius 2.5 mm, inner radius 1.0 mm) indicates that the region where the effective solid penetration depth (optical path) is strictly less than 1 mm constitutes only ~2.02% of the projected width. Consequently, for nearly 98% of the projected area, incident light experiences profound attenuation, making the macroscopic assumption that the occlusion is a completely light-blocking zone a highly accurate and justifiable approximation within the dose model. Based on calculations using **Equation 11** for the printing window in Figure 7B and the absorbance characteristics of the F6 ink, the shell radius was set to 5.0 mm. Accordingly, four structures, BCC, octet truss (OCTET), TPMS, and ring, were designed with a height of 8.0 mm. Figure 7C presents the digital models, printing process, and physical representations of these core–shell multi-material structures.

3.4.2. Analysis of the drug release

Figure 7D–G presents the drug release profiles of the fabricated multi-material DDSs. The release profile indicates that BSA loaded within the pH-responsive hydrogel core exhibited limited release in SGF, with only 16.1% released within the first 2 h and a cumulative release of 47.0% by 48 h. Conversely, in SIF (pH 7.4), 48.4% of the BSA was released within 2 h, achieving 79.9% at 48 h, thereby demonstrating pH-responsive release behavior. Meanwhile, MET incorporated into the non-responsive hydrogel shells was released primarily during the initial 2 h across all geometries. This initial release phase, which corresponds to the typical gastric residence time of oral dosage forms[41], resulted in cumulative MET release exceeding 90% in all cases. The DDSs with varying shell topologies demonstrated release rates in the following order: BCC > TPMS > OCTET > ring. This sequence correlates with the specific surface area of the respective structures, confirming that a larger surface area promotes contact between the drug matrix and the release medium, facilitating dissolution.[50] This finding underscores the ability to program release kinetics by tuning the carrier's macroscopic topology.

The application of the VAM process window and the overprinting strategy enabled the fabrication of a core-shell multi-material DDS. Experimental data indicate that the non-responsive shell facilitates the delivery of small-molecule drugs, while the pH-responsive core provides gastric protection and intestinal release for macromolecular therapeutics. Furthermore, the correlation between shell topology and release rates indicates that geometric design can serve as a tunable parameter for programming release kinetics. These results validate VAM's ability to construct multicomponent systems with site-specific, programmable drug-delivery profiles.

While the current study has successfully established a generalized physical process window and experimentally validated it through cell-free functional DDS, the transition to direct volumetric bioprinting introduces additional optical complexities. From an optical perspective, living cells encapsulated within the bioink fundamentally constitute a population of dynamic light-scattering centers. Consequently, an increase in cell density significantly enhances the bioink's capacity to attenuate incident light. Macroscopically, this phenomenon manifests as an increase in the apparent optical absorbance of the ink, thereby narrowing the printable process window for volumetric bioprinting. Under such conditions, driven by the printing ink's elevated apparent optical absorbance, the risk of surface overcuring near the vat boundary is concurrently amplified. Therefore, elucidating the quantitative relationship between specific cell densities and the apparent optical absorbance of the printing ink and integrating these cell-induced scattering characteristics into the existing theoretical model represents a critical direction for future research.

4. Conclusion

In summary, this study demonstrates that surface overcuring in VAM is governed by the coupled effects of material, process, and hardware parameters rather than any single factor. By developing a generalized theoretical model to predict the spatial light-dose distribution within rotating ink, we showed that lower material absorbance, smaller vat diameters, and narrower projection beams help establish a favorable radial light-dose gradient, thereby suppressing unintended polymerization near the vat boundary. This conclusion was supported by experimental validation. On this basis, a quantitative printing process window was then established to guide the rational design of VAM conditions for complex fabrication tasks. Its practical value was confirmed through the successful fabrication of functional pH-responsive single- and multi-material DDSs with controlled release behavior. These findings broaden the printability of VAM and provide a useful framework for the fabrication of more complex and application-oriented 3D structures.

Acknowledgements

None

Funding

The authors acknowledge the financial support received from the National Key Research and Development program of China (2024YFB4607700), the National Natural Science Foundation of China (52575329), the Science and Technology Innovation Program of Hunan Province (2025RC1026), the Natural Science Foundation of Hunan Province (2025JJ50226), and the Natural Science Foundation of Chongqing (CSTB2023NSCQ-MSX0999).

Conflict of interest

Wei Zhu and Xiaoxiao Han are Editorial Board Members of this journal, but were not in any way involved in the editorial and peer-review process conducted for this paper, directly or indirectly. The authors declare no conflicts of interest.

Author contributions

Conceptualization: Feng Chen, Xiaoxiao Han
Formal analysis: Yifei Wang, Wei Zhu, Yangguang Zhao, Ling Li
Funding acquisition: Feng Chen, Xiaoxiao Han
Investigation: Yifei Wang, Miaomiao Yuan
Methodology: Yifei Wang, Miaomiao Yuan
Writing–original draft: Yifei Wang
Writing–review & editing: Feng Chen, Xiaoxiao Han

Ethics approval and consent to participate

Not applicable.

Consent for publication

Not applicable.

Data availability

Data are available from the corresponding author upon reasonable request.

References

1. Whyte DJ, Doeven EH, Sutti A, Kouzani AZ, Adams SD. Volumetric additive manufacturing: A new frontier in layer-less 3D printing. *Addit Manuf*. 2024;84:104094.

   doi: 10.1016/j.addma.2024.104094

2. Kollep M, Konstantinou G, Madrid-Wolff J, *et al*. Tomographic volumetric additive manufacturing of silicon oxycarbide ceramics. *Adv Eng Mater*. 2022;24(7):2101345.

   doi: 10.1002/adem.202101345

3. Bernal PN, Bouwmeester M, Madrid-Wolff J, *et al*. Volumetric bioprinting of organoids and optically tuned hydrogels to build liver-like metabolic biofactories. *Adv Mater*. 2022;34(15):2110054.

   doi: 10.1002/adma.202110054

4. Toombs JT, Luitz M, Cook CC, *et al*. Volumetric additive manufacturing of silica glass with microscale computed axial lithography. *Science*. 2022;376(6590):308-312.

   doi: 10.1126/science.abm6459

5. Safari H, Hedayati SK, Islam A, Yang Y. Upscaling tomographic volumetric 3D printing via virtual stitching of coordinated projections. *arXiv*. Preprint posted 2025.

   doi: 10.48550/arXiv.2510.07981

6. Zhu Y, Nipu SMA, Chen S, Li X. Linear volumetric additive manufacturing of polymer structures via light initiated direct growth. *Light Adv Manuf*. 2025;6(4):63.

   doi: 10.37188/lam.2025.063

7. Behravesh AH, Tariq A, Buni J, Rizvi G. Computed tomography-based volumetric additive manufacturing: Development of a model based on resin properties and part size interrelationship—Part I. *J Manuf Mater Process*. 2025;9(6):178.

   doi: 10.3390/jmmp9060178

8. Madrid-Wolff J, Boniface A, Loterie D, Delrot P, Moser C. Controlling light in scattering materials for volumetric additive manufacturing. *Adv Sci*. 2022;9(22):2105144.

   doi: 10.1002/advs.202105144

9. Xie M, Lian L, Mu X, *et al*. Volumetric additive manufacturing of pristine silk-based (bio)inks. *Nat Commun*. 2023;14(1):210.

   doi: 10.1038/s41467-023-35807-7

10. Kelly BE, Bhattacharya I, Heidari H, Shusteff M, Spadaccini CM, Taylor HK. Volumetric additive manufacturing via tomographic reconstruction. *Science*. 2019;363(6431):1075-1079.

    doi: 10.1126/science.aau7114

11. Thijssen Q, Toombs J, Li CC, Taylor H, Van Vlierberghe S. From pixels to voxels: A mechanistic perspective on volumetric 3D-printing. *Prog Polym Sci*. 2023;147:101755.

    doi: 10.1016/j.progpolymsci.2023.101755

12. Bernal PN, Delrot P, Loterie D, *et al*. Volumetric bioprinting of complex living-tissue constructs within seconds. *Adv Mater*. 2019;31(42):1904209.

    doi: 10.1002/adma.201904209

13. Chen T, You S, Xu L, *et al*. High-fidelity tomographic additive manufacturing for large-volume and high-attenuation situations using expectation maximization algorithm. *Addit Manuf*. 2024;80:103968.

doi: 10.1016/j.addma.2024.103968

14. Salajeghe R, Garmshausen Y, Arzhangnia Y, *et al*. A numerical framework for modeling the Xolography additive manufacturing method. *Addit Manuf*. 2025;113:105006.

doi: 10.1016/j.addma.2025.105006

15. Kelly B, Bhattacharya I, Shusteff M, Panas RM, Taylor HK, Spadaccini CM. Computed axial lithography (CAL): Toward single step 3D printing of arbitrary geometries. *arXiv*. Preprint published online 2017.

doi: 10.48550/arXiv.1705.05893

16. Regehly M, Garmshausen Y, Reuter M, *et al*. Xolography for linear volumetric 3D printing. *Nature*. 2020;588(7839):620-624.

doi: 10.1038/s41586-020-3029-7

17. Loterie D, Delrot P, Moser C. High-resolution tomographic volumetric additive manufacturing. *Nat Commun*. 2020;11(1):852.

doi: 10.1038/s41467-020-14630-4

18. Zhang Y, Houlahan K, Webber D, *et al*. Advancing tomographic volumetric printing via oxygen inhibition control: Improved accuracy and large-volume capability. *Adv Mater*. 2025;37(47):e08729.

doi: 10.1002/adma.202508729

19. Zhang Y, De Haan H, Houlahan K, *et al*. Impact of oxygen inhibition on (meth)acrylate photopolymerization in tomographic volumetric printing. *Addit Manuf*. 2025;109:104844.

doi: 10.1016/j.addma.2025.104844

20. Pazhamannil RV, Govindan P, Edacherian A. Optimized projections and dose slices for the volumetric additive manufacturing of three dimensional objects. *Mater Today Proc*. 2021;44:922-925.

doi: 10.1016/j.matpr.2020.10.807

21. Webber D, Zhang Y, Picard M, Boisvert J, Paquet C, Orth A. Versatile volumetric additive manufacturing with 3D ray tracing. *Opt Express*. 2023;31(4):5531-5544.

doi: 10.1364/OE.481318

22. Wang F, Li L, Zhu X, Chen F, Han X. Development of pH-responsive polypills via semi-solid extrusion 3D printing. *Bioengineering*. 2023;10(4):402.

doi: 10.3390/bioengineering10040402

23. Lin P, Liu L, He G, *et al*. Preparation and properties of carboxymethyl chitosan/oxidized hydroxyethyl cellulose hydrogel. *Int J Biol Macromol*. 2020;162:1692-1698.

doi: 10.1016/j.ijbiomac.2020.07.282

24. Wu IY, Bala S, Škalko-Basnet N, Di Cagno MP. Interpreting non-linear drug diffusion data: Utilising Korsmeyer-Peppas model to study drug release from liposomes. *Eur J Pharm Sci*. 2019;138:105026.

doi: 10.1016/j.ejps.2019.105026

25. Lotfy VF, Basta AH. Optimizing the chitosan-cellulose based drug delivery system for controlling the ciprofloxacin release versus organic/inorganic crosslinker, characterization and kinetic study. *Int J Biol Macromol*. 2020;165:1496-1506.

doi: 10.1016/j.ijbiomac.2020.10.047

26. Darkes-Burkey C, Shepherd RF. Volumetric 3D printing of endoskeletal soft robots. *Adv Mater*. 2024;36(33):2402217.

doi: 10.1002/adma.202402217

27. Pellizzon N, Šeta B, Kruse CS, Salajeghe R, Spangenberg J. Investigating thermal strains and chemical shrinkage in tomographic volumetric additive manufacturing. *Addit Manuf*. 2025;105:104781.

doi: 10.1016/j.addma.2025.104781

28. Salajeghe R, Meile DH, Kruse CS, Marla D, Spangenberg J. Numerical modeling of part sedimentation during volumetric additive manufacturing. *Addit Manuf*. 2023;66:103459.

doi: 10.1016/j.addma.2023.103459

29. Ribezzi D, Gueye M, Florczak S, *et al*. Shaping synthetic multicellular and complex multi-material tissues via embedded extrusion-volumetric printing of microgels. *Adv Mater*. 2023;35(36):2301673.

doi: 10.1002/adma.202301673

30. Riffe MB, Davidson MD, Seymour G, *et al*. Multi-material volumetric additive manufacturing of hydrogels using gelatin as a sacrificial network and 3D suspension bath. *Adv Mater*. 2024;36(34):2309026.

doi: 10.1002/adma.202309026

31. Ji Y, Su E, Yee D. Volumetric additive manufacturing of composites via hydrogel infusion. *ACS Mater Lett*. 2025;7(8):1021-1030.

doi: 10.1021/acsmaterialslett.5c00407

32. Weisgraber TH, de Beer MP, Huang S, *et al*. Virtual Volumetric Additive Manufacturing (VirtualVAM). *Adv Mater Technol*. 2023;8(23):2301054.

doi: 10.1002/admt.202301054

33. Lü JQ, Sun JS, Jia RP, *et al*. Erosion-free penalty minimization optimization for high-fidelity computed axial lithography. *Addit Manuf*. 2025;111:104990.

doi: 10.1016/j.addma.2025.104990

34. Bami MS, Raeisi Estabragh MA, Khazaeli P, Ohadi M, Dehghannoudeh G. pH-responsive drug delivery systems as intelligent carriers for targeted drug therapy: Brief history, properties, synthesis, mechanism and application. *J Drug Deliv Sci Technol*. 2022;70:102987.

doi: 10.1016/j.jddst.2021.102987

35. Wang L, Gang X, Xiao Y, *et al*. Sodium alginate/carboxymethyl chitosan-CuO hydrogel beads as a pH-sensitive carrier for the controlled release of curcumin. *Eur Polym J*. 2023;192:112069.

doi: 10.1016/j.eurpolymj.2023.112069

36. Jing H, Huang X, Du X, Mo L, Ma C, Wang H. Facile synthesis of pH-responsive sodium alginate/carboxymethyl chitosan hydrogel beads promoted by hydrogen bond. *Carbohydr Polym*. 2022;278:118993.

doi: 10.1016/j.carbpol.2021.118993

37. Zhang Y, Zhao W, Lin Z, Tang Z, Lin B. Carboxymethyl chitosan/sodium alginate hydrogel films with good biocompatibility and reproducibility by in situ ultra-fast crosslinking for efficient preservation of strawberry. *Carbohydr Polym*. 2023;316:121073.

doi: 10.1016/j.carbpol.2023.121073

38. Matricardi P, Di Meo C, Coviello T, Hennink WE, Alhaique F. Interpenetrating polymer networks polysaccharide hydrogels for drug delivery and tissue engineering. *Adv Drug Deliv Rev*. 2013;65(9):1172-1187.

doi: 10.1016/j.addr.2013.04.002

39. Habib M, Berthalon S, Leclercq L, Tourrette A, Sharkawi T, Blanquer S. Dual cross-linked stimuli-responsive alginate-based hydrogels. *Biomacromolecules*. 2024;25(3):1660-1670.

doi: 10.1021/acs.biomac.3c01201

40. Hu Y, Luo Z, Bao Y. Trends in photopolymerization 3D printing for advanced drug delivery applications. *Biomacromolecules*. 2024;26(1):85-117.

doi: 10.1021/acs.biomac.4c01004

41. Lacerda L, Parize AL, Fávere V, Laranjeira MCM, Stulzer HK. Development and evaluation of pH-sensitive sodium alginate/chitosan microparticles containing the antituberculosis drug rifampicin. *Mater Sci Eng C*. 2014;39:161-167.

doi: 10.1016/j.msec.2014.01.054

42. Yuan X, Liu R, Zhang W, *et al*. Preparation of carboxylmethylchitosan and alginate blend membrane for diffusion-controlled release of diclofenac diethylamine. *J Mater Sci Technol*. 2021;63:210-215.

doi: 10.1016/j.jmst.2020.05.008

43. Gao C, Wang XL, An QD, Xiao ZY, Zhai SR. Synergistic preparation of modified alginate aerogel with melamine/chitosan for efficiently selective adsorption of lead ions. *Carbohydr Polym*. 2021;256:117564.

doi: 10.1016/j.carbpol.2020.117564

44. Zhu C, Zhang X, Gan J, *et al*. A pH-sensitive hydrogel based on carboxymethylated konjac glucomannan crosslinked by sodium trimetaphosphate: Synthesis, characterization, swelling behavior and controlled drug release. *Int J Biol Macromol*. 2023;232:123392.

doi: 10.1016/j.ijbiomac.2023.123392

45. Adamov I, Stanojević G, Medarević D, *et al*. Formulation and characterization of immediate-release oral dosage forms with zolpidem tartrate fabricated by digital light processing (DLP) 3D printing technique. *Int J Pharm*. 2022;624:122046.

doi: 10.1016/j.ijpharm.2022.122046

46. Pereira BC, Isreb A, Forbes RT, *et al*. 'Temporary Plasticiser': A novel solution to fabricate 3D printed patient-centred cardiovascular 'Polypill' architectures. *Eur J Pharm Biopharm*. 2019;135:94-103.

doi: 10.1016/j.ejpb.2018.12.009

47. Salajeghe R, Šeta B, Marla D, Spangenberg J. Using viscoplastic fluid to suppress part sedimentation in volumetric additive manufacturing. *Prog Addit Manuf*. 2025;10(4):2411-2422.

doi: 10.1007/s40964-024-00758-y

48. Han X, Wang Y, Chen F, Zhu W, Li J, Wang F. A method and system for volumetric printing of multi-material components. China National Intellectual Property Administration, China Patent CN115107272B. 2023.

49. Boniface A, Maître F, Madrid-Wolff J, Moser C. Volumetric helical additive manufacturing. *Light Adv Manuf*. 2023;4(2):12.

doi: 10.37188/lam.2023.012

50. Kyobula M, Adedeji A, Alexander MR, *et al*. 3D inkjet printing of tablets exploiting bespoke complex geometries for controlled and tunable drug release. *J Control Release*. 2017;261:207-215.

doi: 10.1016/j.jconrel.2017.06.025